



ChemComm

**Development of Defective Molybdenum Oxides for
Photocatalysis, Thermal Catalysis, and Photothermal
Catalysis**

Journal:	<i>ChemComm</i>
Manuscript ID	CC-FEA-05-2022-002658.R1
Article Type:	Feature Article

SCHOLARONE™
Manuscripts

Development of Defective Molybdenum Oxides for Photocatalysis, Thermal Catalysis, and Photothermal Catalysis

Hao Ge,^a Yasutaka Kuwahara,^{*a,b,c} and Hiromi Yamashita^{*a,b}

Received 00th January 20xx,
Accepted 00th January 20xx

DOI: 10.1039/x0xx00000x

The surface plasmon resonance (SPR) of noble metals has been investigated for decades for applications in various catalysis reactions and optical research, but its development has been hampered by inefficient light absorption and high prices. In comparison, the creation of less expensive semiconductors (metal oxides) with strong plasmonic absorption is an appealing option, particularly defective molybdenum oxide (H_xMoO_{3-y}) has received considerable attention and investigation as a promising plasmonic material for a variety of catalytic reactions (photocatalysis, thermocatalysis, photothermal catalysis, etc.). H_xMoO_{3-y} 's SPR effect can be tuned throughout a broad spectrum range from visible to near-infrared (NIR) by altering the doping amount by electrochemical control, chemical reduction, or photochemical control. Notably, defects (oxygen vacancies) in H_xMoO_{3-y} arise in conjunction with the SPR effect, resulting in the formation of unique and useful active sites in a range of catalytic processes. In this review, we explore the formation mechanism of the H_xMoO_{3-y} with plasmonic feature and discuss its applications in photocatalysis, thermocatalysis, and photothermal catalysis.

1. Introduction

Molybdenum oxide is one of the versatile transition-metal-oxide semiconductors with a broad range of applications in thermal materials, electronics, catalysis, sensors, biological systems, and electrochromic systems. Due to their unique properties, MoO_3 is among the most flexible and functional optical and electronic oxides. Importantly, it exists in a variety of stoichiometries, ranging from the full stoichiometry MoO_3 with a large bandgap (ca. 3.0 eV) to the more conductive reduced oxides MoO_{3-x} ($0 < x < 1$). The generation of oxygen vacancies is accompanied by the conversion of Mo^{6+} ions to Mo^{5+} or Mo^{4+} . The optical appearance of molybdenum oxide changes with the degree of reduction, from white to blue and eventually up to black.¹ This changing redox state holds tremendous potential for photocatalysis and thermal catalysis applications.²⁻⁴

For academic research and industrial applications, a variety of synthetic methods (liquid and gas phase) have been developed to synthesize molybdenum-based oxides. By varying the fabrication technique, various nanostructures of molybdenum oxide are achievable, including nanosheets, nanorods, quantum dots, nanobelts, porous nanostructures, and other nano-morphologies.⁵⁻⁹ Typically, crystals of MoO_3 present orthogonal, monoclinic, and hexagonal phases, which are composed of MoO_6 octahedra with side and corner-sharing.¹⁰ The modification of layered MoO_3 intercalation has been widely reported, particularly, using the intercalation of H^+ and alkali ions, which tunes the chemical, physical, and structural properties for expanding the application in energy storage, photochemical, and electrochemical systems.¹¹

Recently, researchers focused on the optical properties of molybdenum oxide, in which defect states were introduced by intercalating H^+ ions into the layers, thereby affecting the optical absorption and photocatalytic activity of MoO_3 .¹² Meanwhile, the generation of oxygen vacancies in molybdenum oxide facilitates the adsorption of reaction substrates (H_2O , CO_2 , N_2 , etc.), leading to a reduction in the reaction energy barrier and an enhancement of the catalytic activity.¹³⁻¹⁵ Furthermore, a novel localized surface plasmon resonance (LSPR) effect is established on hydrogen-doped MoO_3 as a result of the increased surface free electron concentration, exhibiting a promising application in plasmonic-assisted photothermal catalysis.¹⁶⁻²⁰ Importantly, plasmonic semiconductors, unlike conventional plasmonic metals, can modulate the shape, size, type of dopant, and dopant concentration of the semiconductor using a combination of chemical, photochemical, and electrochemical methods to alter the free carrier concentration, overall electron scattering, and surrounding near-field enhancement within the nanocrystal to achieve a tunable LSPR effect. Moreover, when a sufficient number of hydrogen atoms are intercalated, defective H_xMoO_{3-y} exhibits a broader plasmonic absorption in the visible region.²¹

Despite growing interest in molybdenum oxide and a large body of research on the material, comprehensive studies of MoO_3 for environmental catalysis remain rare. This paper focuses on the nanostructure, defect engineering, and optical characteristics of molybdenum oxide, summarizes its applications by utilization of plasmonic effects, oxygen vacancy, and photothermal effects to alleviate environmental and energy crises, and provides theoretical knowledge for future understanding and exploitation of molybdenum oxide materials.

2. Fundamental properties

2.1 Crystal structures of MoO_3

Molybdenum oxides and their hydrated compounds are quite structurally diverse (Fig. 1), in which the orthorhombic phase

^a Division of Materials and Manufacturing Science, Graduate School of Engineering, Osaka University, 2-1 Yamada-oka, Osaka 565-0871, Japan. E-mail: kuwahara@mat.eng.osaka-u.ac.jp; yamashita@mat.eng.osaka-u.ac.jp

^b Innovative Catalysis Science Division, Institute for Open and Transdisciplinary Research Initiatives (OTRI), Osaka University, 2-1 Yamada-oka, Suita, Osaka 565-0871, Japan

^c JST, PRESTO, 4-1-8 Hon-Cho, Kawaguchi, Saitama 332-0012, Japan



Hao Ge received his master degree in chemistry and materials science from Shanghai Normal University in 2019. He is currently a PhD course student in the department of engineering in Osaka University. His current research interests focus on the plasmonic photothermal catalytic CO₂ conversion based on molybdenum-based catalysts.



Yasutaka Kuwahara received his PhD degree in engineering from Osaka University in 2011. After the fellowship, he was a researcher at National Institute of Advanced Industrial Science and Technology (AIST), Japan, in 2012–2014. He was appointed as an assistant professor at Osaka University in 2014–2019, appointed as a lecturer in 2019, and has been an associate professor since 2021. His current research

interests include the design of nanostructured catalysts with multi-functionalities using porous materials and their applications to green chemical reactions and the conversion of energy and resources.



Hiromi Yamashita has been a professor at Osaka University since 2004. He received a PhD degree from Kyoto University in 1987. He was an assistant professor at Tohoku University and an associate professor at Osaka Prefecture University. He has been the editor of *Applied Catalysis B: Environmental* (2006–), the president of Asia-Pacific Association of Catalysis Societies (2019–), the president of Catalysis

Society of Japan (2019–2020), His research interests include the design of single-site photocatalysts and nanostructured catalysts.

and the sub-stable monoclinic phase are the two most prevalent structural phases of MoO₃ based on the MoO₆ octahedral structural block, each with unique physicochemical properties. In addition, ε-MoO₃ and the relatively stable hexagonal phase h-MoO₃ are also well-known.^{22–24} The unique layered crystal structure of orthorhombic α-MoO₃ offers the possibility of building two-dimensional (2D) morphologies that have gained widespread attention in catalytic reactions. The layers consist of a double layer of edge-sharing and distorted MoO₆ octahedra with a thickness of 0.7 nm. The distance between the two layers is 1.4 nm. In the [001] direction, planar double-layer sheets of distorted MoO₆ octahedra create zigzag rows; in the [100] direction, corner-sharing rows form.²⁵ The deformed MoO₆ octahedra are connected vertically [010] by weak van der Waals (vdW) forces, resulting in stratification, while their interior interactions are governed by strong covalent and ionic bonds (Fig. 2a).^{26–28} The electronic energy band structure of DFT-HSE06 in Fig. 2b reveals that the valence and conduction bands of α-MoO₃ are composed of O 2p states and

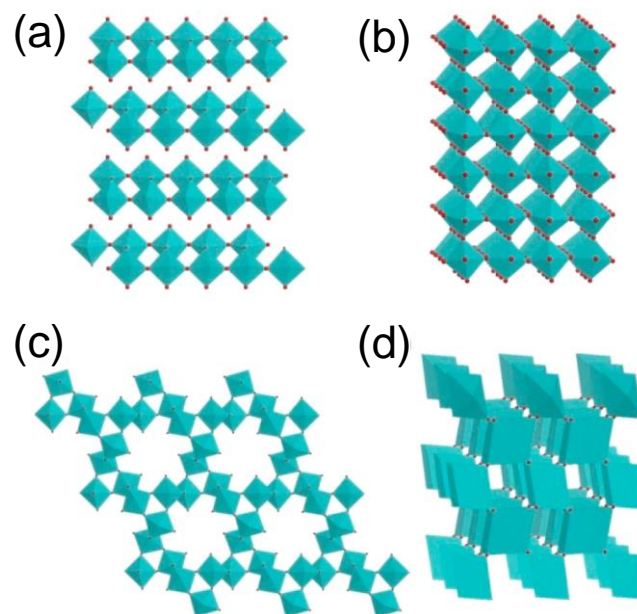


Fig. 1 The atomic structure of molybdenum oxide in various crystalline phases. (a) α-MoO₃, (b) β-MoO₃, (c) h-MoO₃, (d) MoO₂. The red sphere represents the oxygen atom. Reproduced with permission from ref. 23. Copyright © 2009 American Chemical Society.

hybridized states of Mo 4d and O 2p, respectively. In part of the electron density, the contribution of Mo atoms is very limited except for the conduction band, whereas oxygen orbitals can be found near both band edges simultaneously. Remarkably, oxygen atoms with common corners and edges contribute significantly more to the 2p orbitals than oxygen atoms near the vertical vdW layer.^{25,29}

2.2. H⁺-doping in α-MoO₃

Owing to the layered structure, α-MoO₃ as a host is suitable to accommodate a large number of guest ions (e. g. Li⁺, H⁺) without the crystal structure being affected.^{30,31} Mai *et al.* revealed that lithiated MoO₃ nanobelts have significantly increased conductivity and electroactivity as compared to unlithiated MoO₃ nanobelts.³² As the smallest ion in nature, H⁺ is an ideal dopant because of its capacity to migrate rapidly into the interstitial locations of inorganic compounds with van der Waals gaps, with theoretical H⁺/MoO₃ ratios as high as 2:1.³³ The intercalated H⁺ ion layers are typically connected to the terminal oxygen atoms of the distorted MoO₆ octahedra, which are located at the van der Waals gaps between the double layers of the α-MoO₃ crystal structure or at the intralayer locations of the zigzagging chains that run along the channels.³⁴ As shown in Fig. 3a, H_xMoO₃ exhibits three thermodynamically stable phases, depending on the intercalated H⁺ concentration.³⁵ In type 1, the intercalated H⁺ is topological and maintains the orthorhombic crystalline phase. However, as the amount of H⁺ in the intercalated layers increases, type 2 and type 3 H_xMoO₃ undergo a phase transition from orthorhombic to monoclinic crystals.³⁶ The H⁺-doping affects the electronic structure of α-MoO₃, causing the high-valence Mo⁶⁺ species to be reduced to Mo⁵⁺ and Mo⁴⁺ species, and ultimately the formation of quasi-metals due to the partial

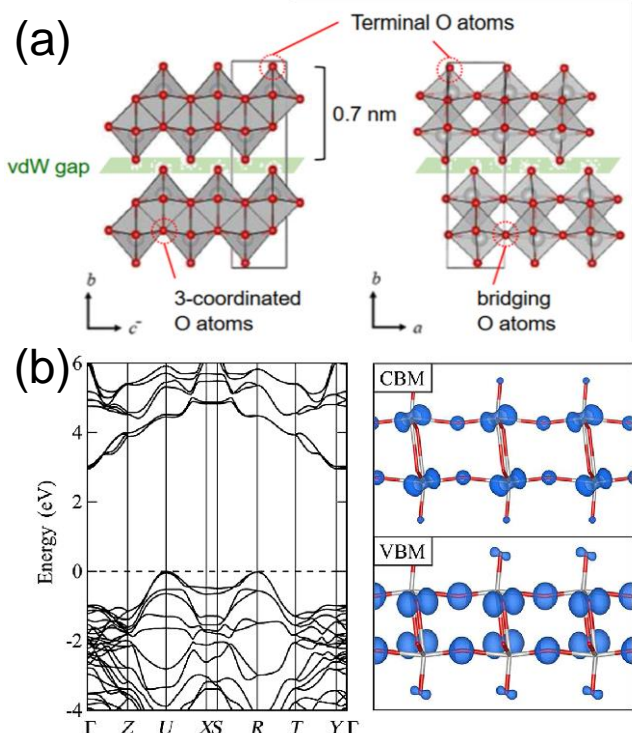


Fig. 2 (a) Atomic and crystal structure of the various MoO_3 polymorphs $\alpha\text{-MoO}_3$, (b) DFT-HSE06 electronic band structures of $\alpha\text{-MoO}_3$. Reproduced with permission from ref. 25. Copyright © 2017 American Physical Society.

filling of the Mo 4d orbital.^{37–39} The formation of H_xMoO_3 is accompanied by the injection of a large number of delocalized electrons, thus producing surface plasmon resonances in the visible light region.^{40,41} Significantly, the H_xMoO_3 surface behaves with highly reversible redox properties, which means that it has high-performance catalytic activity for chemicals with the appropriate redox potential.⁴² Fujishima *et al.* reported the synthesis of visible-light-sensitive reversible photochromic films of MoO_3 , revealing a reversible redox event in the Mo atom by controlling the storage and release of free electrons. Firstly, the $\alpha\text{-MoO}_3$ film produces a strong colour enhancement (deep blue) when irradiated with visible light in the air, displaying a distinct visible absorption peak in the UV-vis NIR spectrum (**Fig. 3b**). Photochromism can be eliminated using subsequent anodic polarization, and the process of coloration and decoloration can be repeated for at least five cycles (**Fig. 3c**).⁴³ Apart from photochemical processes, electrochemical reactions can drive color changes in $\alpha\text{-MoO}_3$ by injecting a certain number of positive ions (M^+) and an equal number of electrons (e^-) (Reaction: $\text{MoO}_3 + x\text{M}^+ + xe^- \rightarrow \text{M}_x\text{MoO}_3$),⁴⁴ which can be attributed to the formation of local Mo^{5+} defect states and the transfer of valence charges between $\text{Mo}^{5+}/\text{Mo}^{6+}$ leads to strong absorption of H_xMoO_3 in the visible light range. Notably, as evidenced by the formation of water during hydrogen intercalation, the molybdenum bronze H_xMoO_3 eventually loses oxygen atoms along with H ions to form defective $\text{H}_x\text{MoO}_{3-y}$.^{45,46}

2.3 Plasmonic effect of non-stoichiometric $\text{H}_x\text{MoO}_{3-y}$

Plasmonic effects in heavily doped transition metal oxides with unique optoelectronic properties have garnered substantial

interest in the past decade. By altering the doping level and electrochemical potential in semiconductors, SPRs can be made inherently adjustable, conferring plasmonic absorption at visible, near-infrared (NIR), and mid-infrared wavelengths (**Fig. 4a**), enabling extremely active catalytic performance in these spectral regions.⁴⁷ In noble metals, collective oscillations originating from free electrons or holes result in improved optical absorption and scattering, as well as a significant near-field amplification at the nanoparticles' surfaces.^{48,49} In order to exhibit the optical properties of metals, doped semiconductors should possess a negative real part of their dielectric function. This requirement is fulfilled when the critical free carrier concentration is exceeded, which is determined by the material's electrical structure, including the effect of defect states. Numerous oxide semiconductors with a wide bandgap can exceed the threshold for metal optical behavior by introducing oxygen defects. Because of the considerable concentration of free electrons in non-stoichiometric $\text{H}_x\text{MoO}_{3-y}$, its absorption in the visible light range has been attributed to the SPR effect.^{50–52} Benefiting from its small diameter and ambivalent character, hydrogen atoms can be intercalated into $\alpha\text{-MoO}_3$ and stored as electron donors or acceptors either in the conduction band or in the defect, serving as the source of plasmonic and electronic effects. The model of hydrogen-doped $\alpha\text{-MoO}_3$ in **Fig. 4b** depicts the electronic structure of $\text{H}_x\text{MoO}_{3-y}$. The unchanging MoO_6 octahedron determines the general electronic structure in this model, but the doping of H atoms results in the introduction of new bandgap states.⁵³ The pristine $\alpha\text{-MoO}_3$ consists of Mo^{6+} forming the conduction band and O^{2-} forming the valence band with a bandgap of 3.2 eV. H atoms contribute their electrons to the conduction band, creating

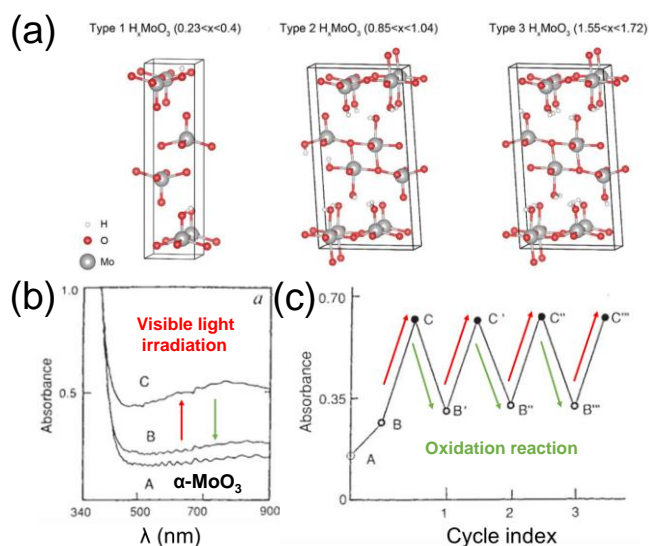


Fig. 3 (a) Three crystal structures doped with different H^+ concentrations: H_xMoO_3 with OH groups (type 1); H_xMoO_3 with OH and OH_2 groups (type 2); H_xMoO_3 with OH and OH_2 groups (type 3). Copyright © 2018 WILEY-VCH Verlag GmbH & Co. KGaA, Weinheim. (b) UV-vis-NIR spectra of the MoO_3 : (curve A) original sample; (curve B) after polarization at -0.1 V versus Ag/AgCl ; (curve C) using visible light to irradiate the sample of curve B for 10 mins. (c) The absorbance change of MoO_3 at 800 nm during visible light irradiation and oxidation reaction. Reproduced with permission from ref. 35, 43. Copyright © 1992 Nature Publishing Group.

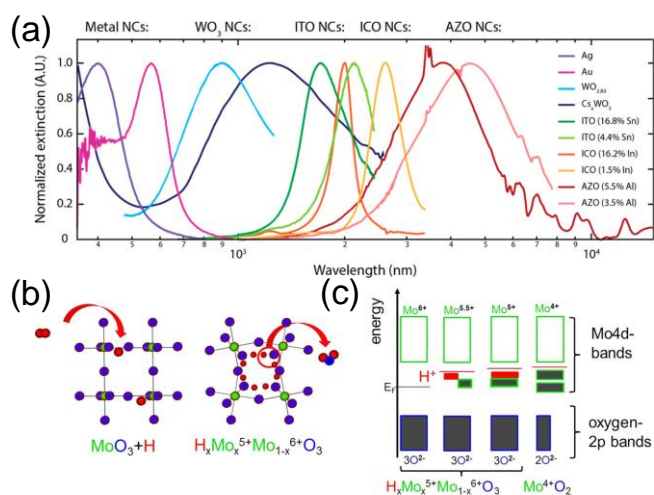


Fig. 4 (a) Normalized optical extinction due to SPRs of metal and metal oxide nanocrystals. Copyright © 2018 American Chemical Society. (b) Crystal structure of MoO₃ and H_xMoO_{3-y}. (c) Electronic-band-structure regulation of MoO₃ by H⁺ intercalation. Reproduced with permission from ref. 47, 55. Copyright © 2017 Springer Nature.

protons and the "valence band-like Mo⁵⁺ state" (Fig. 4c: green/grey state in the bandgap). The colour of the hydrogenated α -MoO₃ film transforms from white to blue by spaced charge transfer between adjacent Mo⁵⁺/Mo⁶⁺ under photoexcitation. Mo⁴⁺ ions are formed when the doping level of hydrogen in the H_xMoO_{3-y} exceeds $x = 1$ (Fig. 4c: width of the electronic states), resulting in the formation of water and hydrogen-free MoO₂, consisting of Mo⁴⁺ and O²⁻ states. Each absent oxygen atom is balanced by two electrons in the Mo 4d band.^{54,55} Yamashita *et al.* developed a plasmonic Pd/H_xMoO_{3-y} hybrid based on the H-spillover process.⁵⁶ In addition, by controlling the H₂ reduction temperature, the stoichiometric compositions of MoO₃ can be adjusted, realizing tunable plasmonic absorption. As shown in Fig. 6a, the hydrogen-doped MoO₃ is obtained via the facile H-spillover process, in which the hydrogen molecules adsorbed on Pd are transformed into activated hydrogen atoms after dissociation, and subsequently, migrate to the surface of molybdenum oxide and intercalate into the bulk, causing the reduction of MoO₃. Compared with the unreduced Pd/MoO₃, Pd/H_xMoO_{3-y}(RT) displays a distinct absorption peak in the visible light region (Fig. 6b). The first principles DFT calculation system was performed to investigate the electronic structures of the hydrogen bronzes. The total density of states (TDOS) and projected density of states (PDOS) of pristine MoO₃ (Fig. 6c) show that there is no defect in the pristine MoO₃, and the bandgap between them is around 1.9 eV. In contrast, the heavily doped hydrogen-molybdenum bronze (H_{1.68}MoO₃) exhibits metallic properties in which the valence band (VB) continuously crosses the fermi energy level into the conduction band (CB) (Fig. 6d).

The change in the electronic structure of the hydrogen-molybdenum bronze is caused by the insertion of hydrogen atoms into the MoO₃ matrix. The layered structure of the orthorhombic α -MoO₃ allows the insertion of a substantial number of H atoms in interlayer positions, which are intensely coordinated with the terminal oxygen atoms, resulting in the

deformation of the MoO₆ octahedra in the H_{1.68}MoO₃ framework (Fig. 6e). The H atoms become protons upon adsorption on the terminal oxygen atoms, and electrons are transferred from H 1s orbitals to O 2p orbitals.⁵⁷ Subsequently, the charge transfer from the terminal oxygen atom to the coordinating Mo atom leads to a partial reduction of the Mo ion. The electron charge density distribution of H_{1.68}MoO₃ (Fig. 6f) shows that the introduced electron charges are uniformly distributed on the Mo atoms, indicating the delocalization properties of Mo 4d electrons. The preceding results indicate that the intercalation of hydrogen ions into MoO₃ allows a significant number of free electrons to be stored in the Mo 4d orbital, enabling an SPR effect in the visible region.⁵⁸

3. Application of α -MoO₃

3.1 The Mechanism of Plasmonic Photocatalysis

Localized surface plasmon resonance (LSPR) originates from the coherent oscillation of conduction band electrons in a catalyst (e.g., metal or semiconductor) when the frequency of the incident light coincides with the frequency of the surface electrons. Excitation by LSPR provides a powerful local electromagnetic field that increases the photon absorption rate of the catalyst (Figure 5a).⁵⁹ Subsequently, plasmon-mediated excitation of the high-energy charge carrier is involved in the reaction of the adsorbed reactants on the catalyst surface, driving photochemical and solar energy conversion. (Figure 5b). Furthermore, in plasmonic metal/semiconductor hybrids, the plasmonic effect improves the yield of hot electrons with high potential energy on the plasmonic metal, thereby aiding the transit of hot electrons to the semiconductor. The Schottky barrier (SB) at the metal/semiconductor interface prevents transported hot electrons from returning to the noble metal to recombine with the hot hole. This design enhances the lifetime

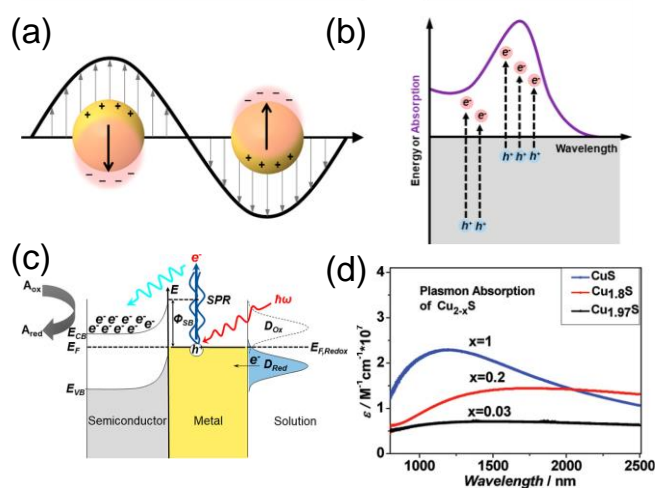


Fig. 5 (a) Schematic illustration of LSPR effect in plasmonic materials. (b) Hot carrier generation and the corresponding absorption spectrum of plasmonic metals. (c) Plasmonic metal/semiconductor compound structures that transfer and utilize LSPR-induced hot electrons to facilitate surface reduction reactions. Copyright © 2018 American Chemical Society. (d) NIR spectra of prepared Cu_{2-x}S NCs: CuS ($x = 1$), Cu_{1.8}S ($x = 0.2$), and Cu_{1.97}S ($x = 0.03$). Copyright © 2009 American Chemical Society. Reproduced with permission from ref. 108, 67.

ARTICLE

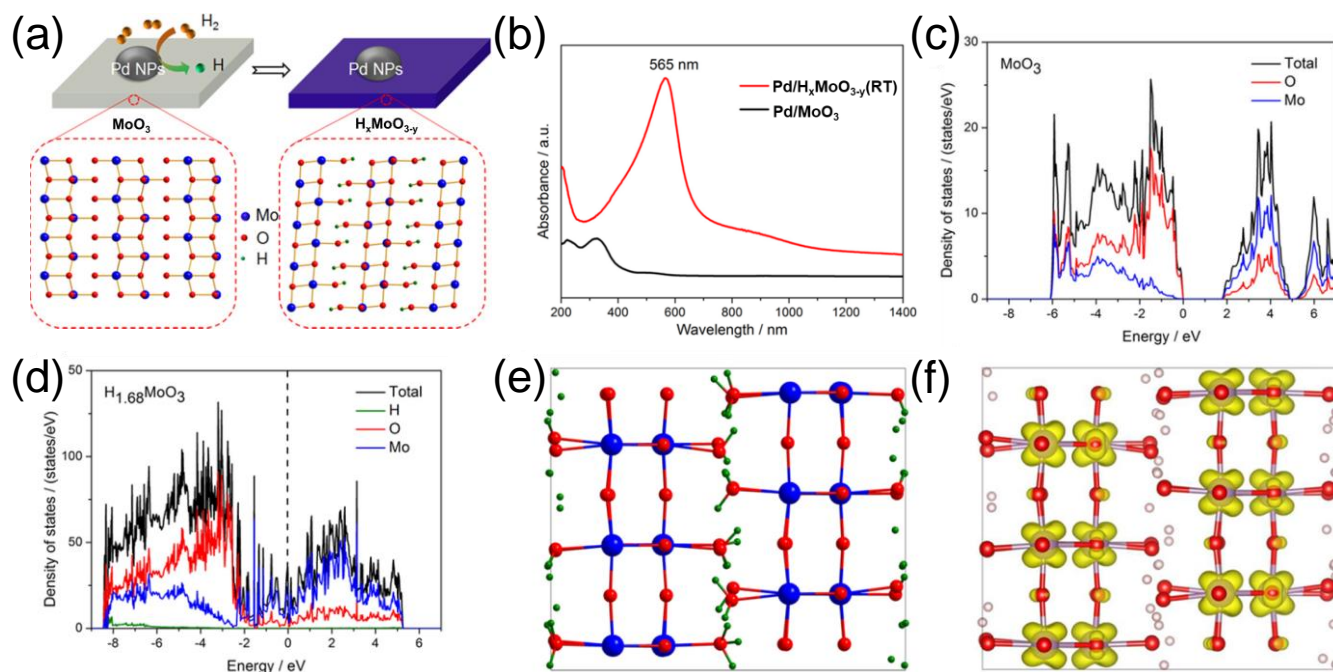


Fig. 6 (a) Schematic illustration of the hydrogen bronze formation process via H-spillover. (b) UV-vis-NIR diffuse reflectance spectra. TDOS and PDOS of (c) pristine MoO_3 and (d) heavily H-doped $\text{H}_x\text{MoO}_{3-y}$. (e) Illustration of the structure of $\text{H}_x\text{MoO}_{3-y}$ in the (010) projection. Blue balls are Mo atoms, red for O, and green for H atoms. (f) Three-dimensional depiction of Fermi level electronic charge density distribution for $\text{H}_x\text{MoO}_{3-y}$.⁵⁶

of the hot electrons transferred to the CB of the semiconductor. Consequently, various surface chemical processes can be enhanced (Fig. 5c), including H_2O splitting, CO_2 reduction, and organic matter conversion.⁶⁰ Linic *et al.* have long been dedicated to research on the promotion of plasmonic metals in photocatalytic water splitting (hydrogen and oxygen evolution), demonstrating the transfer mechanism of plasmon-induced hot electrons, in which hot electrons migrate into the semiconductor to improve charge separation efficiency and thus photocatalytic activity.^{61–63} Similar catalytic behavior is also found in plasmonic non-metallic catalysts (e.g., BiO_{3-x} , WO_{3-x} , and $\text{In}_2\text{O}_{3-x}$).^{64–66} Cu_{2-x}S as a plasmonic semiconductor catalyst, where the collective oscillations of free charge carriers on the valence band drive the LSPR, the plentiful free electrons are attributed to the Cu vacancy production during the synthesis process.⁶⁷ In addition, the Cu_{2-x}S nanomaterials exhibit LSPR effects in the NIR and mid-IR areas compared to noble metals (Fig. 5d) due to the lower order of magnitude of free electrons in them. And then the generated hot electrons will transfer to nearby structures at the level of unoccupied acceptor molecules and induce chemical transformations.⁶⁸

3.1.1 Applications of $\text{H}_x\text{MoO}_{3-y}$. The plasmonic non-metallic catalysts absorb photons from solar, inspire photogenerated charges (e^- and h^+) and transport them to the surface of the catalytic reaction active sites for efficient photocatalytic reactions. Yamashita's group has achieved some significant results in relevant fields. They synthesized blue $\text{H}_x\text{MoO}_{3-y}$ nanosheets by a simple solvothermal method in the

absence of surfactant, exhibiting SPR absorption in the visible region.⁶⁹ The obtained blue $\text{H}_x\text{MoO}_{3-y}$ nanosheets have very stable chemical properties, which maintain the color in the air for several months. The X-ray diffraction pattern shows that the as-prepared molybdenum oxide is assigned as an orthorhombic phase, which has a layered structure composed of MoO_6 octahedra. Ethanol as a solvent has strong reducibility during the synthesis process, which produced H-doped molybdenum oxide, causing sufficient free carriers to sustain the SPR effect. XPS results display that a new peak assigned to Mo^{5+} species appears in the $\text{H}_x\text{MoO}_{3-y}$ nanosheets, demonstrating the intercalation of H atoms. The as-prepared $\text{H}_x\text{MoO}_{3-y}$ exhibits a strong plasmonic absorption peak in the visible range, and the plasmonic absorption region is tunable from the visible to the near-infrared range by changing alcohols used in the solvothermal synthesis (Fig. 7a). By virtue of its strong plasmonic effect, $\text{H}_x\text{MoO}_{3-y}$ exhibits high hydrogen production activity in photocatalytic ammonia-borane (NH_3BH_3) hydrogen production reactions. The initial H_2 production on $\text{H}_x\text{MoO}_{3-y}$ was 3.7 times faster than that of MoO_3 (Fig. 7c). Even in dark conditions, the $\text{H}_x\text{MoO}_{3-y}$ still presents the highest activity rates (Fig. 7b). Such positive results are attributed to the significant number of free electrons on the surface of the $\text{H}_x\text{MoO}_{3-y}$, which play a crucial role in hydrogen production.⁷⁰ However, the preferential production of 2D MoO_3 nanosheets during the synthesis resulted in a limited surface area and relatively low catalytic activity, restricting the use of surface free electrons. Therefore, a high surface area MoO_3 was prepared by adding a surfactant

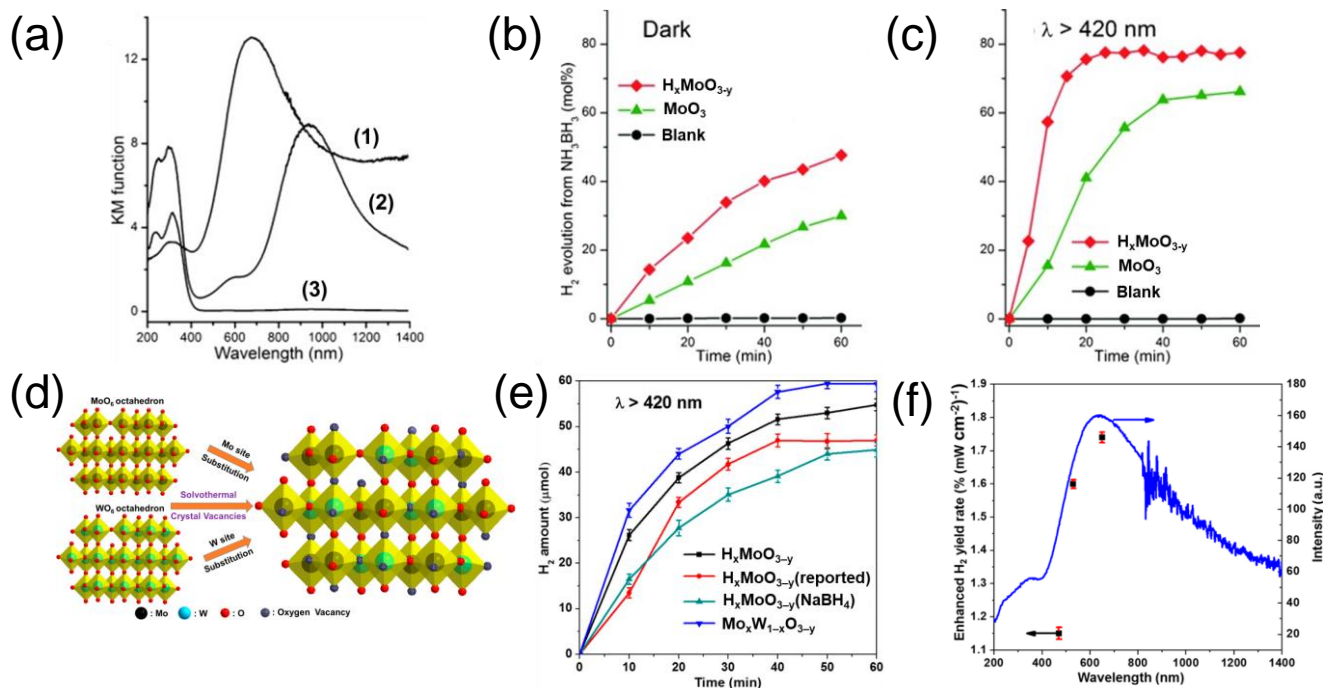


Fig. 7 (a) UV/Vis–NIR diffuse reflectance spectra of the H_xMoO_{3-y} samples prepared at 160 °C (1) and 140 °C (2) for 12 h, and commercial MoO_3 (3). H_2 production test from aqueous NH_3BH_3 solutions at room temperature. (b) in the dark and (c) under visible light irradiation ($\lambda > 420$ nm).⁶⁹ (d) Illustration of the possible formation process of crystal defects in $Mo_xW_{1-x}O_{3-y}$. (e) H_2 evolution from NH_3BH_3 at room temperature of different materials. (f) Wavelength-dependent initial H_2 yield rate enhancement of $Mo_xW_{1-x}O_{3-y}$ samples upon irradiation by LED light.⁷⁵

to the solvent using an evaporation-induced self-assembly (EISA) process.⁷¹ By injecting heterovalent atoms into semiconductor crystals, doped semiconductors such as aluminum, germanium, indium-doped zinc oxide, and indium-doped tin oxide (ITO) can be synthesized rapidly and efficiently, changing the light absorption intensity and range of their SPR effect.^{72–74} We synthesized a plasmonic $Mo_xW_{1-x}O_{3-y}$ material with intense SPRs in the visible light range by a facile non-aqueous solvothermal method (Fig 7d). Comprehensive analysis revealed that the molybdenum and tungsten ion inter-doping vacancies, as well as the oxygen vacancies formed during crystal growth, are the primary causes responsible for the catalyst's strong plasmonic absorption. Under visible light irradiation ($\lambda > 420$ nm), the obtained plasmonic $Mo_xW_{1-x}O_{3-y}$ acted as an effective catalyst, greatly increasing the dehydrogenation activity of ammonia borane, with the best performance under the light irradiation at $\lambda = 650$ nm (Fig 7e, f).⁷⁵

3.1.2 Applications of metal- H_xMoO_{3-y} hybrids. Single-component materials frequently fail to satisfy the catalytic requirements in heterogeneous photocatalysis due to their intrinsic constraints of limited light absorption and low catalytic efficiency.^{76,77} Hybrid materials, as composite materials possessing synergistic multiple coupling effects, offer greater potential in catalytic applications. Chen *et al.* developed a plasmonic Pd/ H_xMoO_{3-y} hybrid via a solution-processed route (NaBH₄ reduction) (Fig. 8a), which displays a strong SPR peak in the visible light region (Fig. 8b). The SPR of the Pd/ H_xMoO_{3-y} hybrid material exhibits reversible tunability under O₂ oxidation

and NaBH₄ reduction conditions (Fig. 8c). Furthermore, the hybrid of Pd/ H_xMoO_{3-y} exhibits significant plasmon-enhanced catalysis in NH₃BH₃ hydrolysis and Suzuki-Miyaura coupling

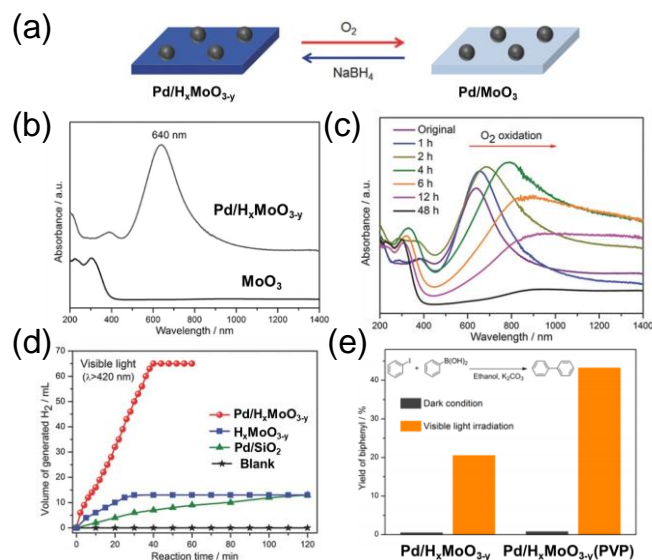


Fig. 8 (a) Schematic illustration of the Pd/ H_xMoO_{3-y} hybrid presenting a redox process in O₂ atmosphere and NaBH₄ solution, respectively. (b) UV-vis-NIR spectra of the Pd/ H_xMoO_{3-y} hybrid and pure MoO_3 , (c) the evolution of the optical response of Pd/ H_xMoO_{3-y} hybrid exposed to air, (d) H_2 production rate from NH_3BH_3 solution under light irradiation ($\lambda > 420$ nm), and (e) the catalytic activity of the Suzuki-Miyaura coupling reaction in dark condition and under light irradiation ($\lambda > 420$ nm).⁷⁹

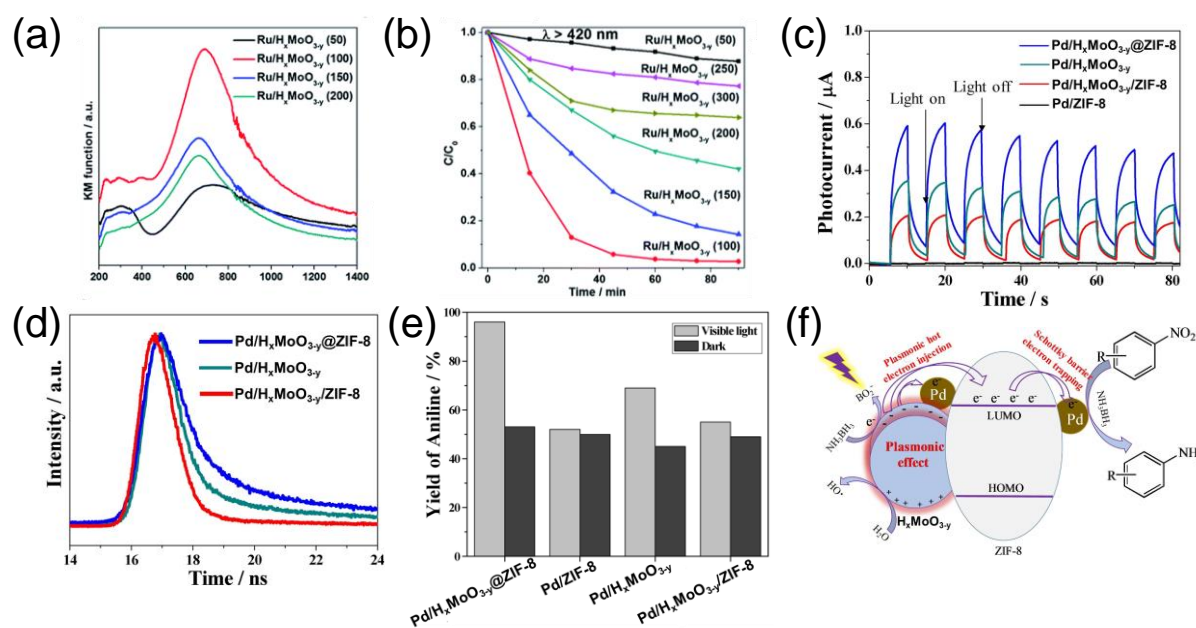


Fig. 9 (a) UV-vis-NIR diffuse reflectance spectra, and (b) plot of relative concentration of *p*-nitrophenol over $\text{Ru}/\text{H}_x\text{MoO}_{3-y}$ (T °C) catalysts reduced at different temperatures.⁷⁶ (c) Photocurrent responses of different samples, (d) time-resolved transient PL decay curves of different samples. (e) The activity of reduced nitrobenzene over different samples under light and dark conditions, respectively. (f) A possible reaction mechanism for the reduction of nitrobenzene derivatives over plasmonic $\text{Pd}/\text{H}_x\text{MoO}_{3-y}@ZIF-8$.⁸⁵

reactions under visible light, being well beyond that of the single-component $\text{H}_x\text{MoO}_{3-y}$ (**Fig. 8 d, e**).⁷⁹ For the efficient photocatalytic conversion of *p*-nitrophenol (PNP) to *p*-aminophenol (PAP), a $\text{Ru}/\text{H}_x\text{MoO}_{3-y}$ hybrid with a plasmonic effect and abundant oxygen vacancies has been developed based on the H-spillover process.⁸⁰ This hybrid is capable of effectively trapping aromatic nitro compounds and weakening the N-O bond, thereby providing an abundance of localized electrons for the reduction reaction. Notably, by changing the H_2 reduction temperature, the plasmonic absorption range of hybrids can be adjusted (**Fig. 9a, b**). We also synthesized $\text{RuPd}/\text{H}_x\text{MoO}_{3-y}$ hybrids to further improve the efficiency of photocatalytic conversion of PNP, in which RuPd alloy nanoparticles and plasmonic $\text{H}_x\text{MoO}_{3-y}$ serve as the active and electron donor centers, respectively, resulting in a synergistic effect in the reaction.⁸¹ However, because rapid recombination of plasmon-excited charge carriers makes it difficult to boost catalytic activity, it is critical to construct viable multiphase complexes that produce heterojunctions or overcome Schottky barriers for effective charge separation and transfer.⁸²⁻⁸⁴ Thus, we presented an interesting approach to improve the utilization of plasmon-induced electrons in photocatalytic nitroaromatic hydrogenation by combining plasmonic $\text{H}_x\text{MoO}_{3-y}$ with $\text{Pd}/\text{ZIF-8}$.⁸⁵ The complexes of Pd nanoparticles with plasmonic $\text{H}_x\text{MoO}_{3-y}@ZIF-8$ contributed synergistically to the promotion of plasma-induced hot-electron transfer, increasing the catalytic activity. The photoelectrochemical tests and time-resolved transient PL decay spectroscopy showed that the $\text{Pd}/\text{H}_x\text{MoO}_{3-y}@ZIF-8$ exhibits the strongest photocurrent density under intermittent illumination and the longest lifetime of hot electrons compared with other samples (**Fig. 9c, d**), demonstrating that the novel structure of $\text{Pd}/\text{H}_x\text{MoO}_{3-y}@ZIF-8$ effectively facilitates plasmon-excited electron transfer and lifetime. Thus, complexes of $\text{Pd}/\text{H}_x\text{MoO}_{3-y}@ZIF-8$ displayed the best activity performance in

the nitrobenzene hydrogenation reaction under visible light irradiation (**Fig. 9e**), and a possible reaction mechanism is proposed based on the transfer pathway of plasmon-excited electrons (**Fig. 9f**). Additionally, the abundance of oxygen vacancies on the surface of metal- $\text{H}_x\text{MoO}_{3-y}$ hybrids also plays a crucial role in catalysis. Kuwahara *et al.* demonstrated for the first time that defective $\text{Pt}/\text{H}_x\text{MoO}_{3-y}$ exhibits high catalytic activity for the deoxygenation of sulfoxide at ambient temperature under 1 atm H_2 , with significantly higher catalytic activity when visible light is introduced compared to the dark environment (**Fig. 10a, c, d**), and the plasmonic absorption of the $\text{Pt}/\text{H}_x\text{MoO}_{3-y}$ was controlled by adjusting the H_2 reduction

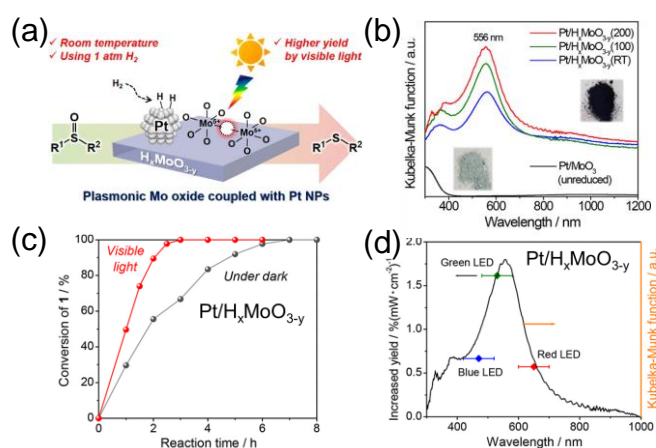


Fig. 10 (a) Sulfoxide deoxygenation reaction mechanism over $\text{Pt}/\text{H}_x\text{MoO}_{3-y}$ hybrid catalyst, (b) UV-vis-NIR diffuse reflectance spectra for the $\text{Pt}/\text{H}_x\text{MoO}_{3-y}$ hybrids with different H_2 reduction temperature, (c) time course in the sulfoxide deoxygenation over $\text{Pt}/\text{H}_x\text{MoO}_{3-y}$ in the dark and under visible light irradiation, (d) the increased yield of activity as a function of the wavelength by LED irradiation.⁷⁸

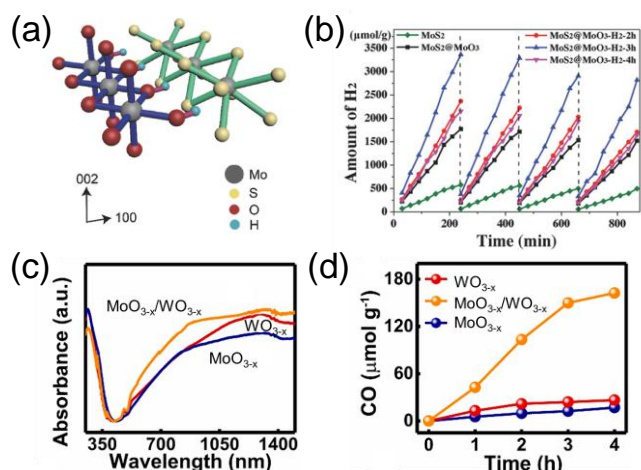


Fig. 11 (a) The nanostructure of the prepared $\text{MoS}_2@\text{MoO}_3\text{-H}_2\text{-7}$ nanostructure, and (b) photocatalytic hydrogen yield over the $\text{MoS}_2@\text{MoO}_3$. Copyright © 2018 WILEY-VCH Verlag GmbH & Co. KGaA, Weinheim. (c) UV-vis-NIR spectra, and (d) the total number of electrons consumed during CO_2 photoreduction. Copyright © 2021 Elsevier. Reproduced with permission from ref. 92, 93.

temperature (Fig. 10b). Related analyses indicate that the oxygen vacancies formed by the H spillover process are the reaction's primary active sites, while the Mo atoms' reversible redox behavior and high plasmonic absorption make a significant contribution to the reaction's activity.⁷⁸

3.1.3 Heterojunctions with $\text{H}_x\text{MoO}_{3-y}$. The fabrication of two-dimensional semiconductor heterostructures has tremendous potential for photocatalytic materials, where the heterojunction's electrical structure is tailored to enhance light absorption and photogenerated carrier separation.^{86,87} After analyzing 2D $\text{MoO}_{3-x}\text{S}_x/\text{MoS}_2$ heterostructures using density flooding theory (DFT) calculations of the HSE06 functional, Bahers *et al.* discovered a type II heterojunction in which the bandgap and charge transfer between the MoO_3 and MoS_2 layers are constantly driven by the S concentration in the $\text{MoO}_{3-x}\text{S}_x$ single layer, providing an efficient direct Z-type system for photocatalytic water splitting.⁸⁸ Liu *et al.* grew 0D CdS nanoparticles on two-dimensional plasmonic MoO_{3-x} using a simple co-precipitation approach. The $\text{CdS}/\text{MoO}_{3-x}$ heterojunction enhances light absorption from 600 nm to 1400 nm by utilizing the SPR effect of MoO_{3-x} and speeds up the separation of photogenerated electrons and holes. As a result, $\text{CdS}/\text{MoO}_{3-x}$ heterojunctions present a higher photocatalytic hydrogen production rate than pure CdS when irradiated by monochromatic light at 420, 450, 550, and 650 nm, as well as improved photocorrosion properties.⁸⁹ The hydrogen reduction process can achieve tunable plasmonic absorption and energy band structure in MoO_3 , allowing for better energy band alignment with the composite semiconductor material and thereby increasing photoinductive electron production in the heterostructure.^{90,91} In view of this, Wei *et al.* produced stable $\text{MoO}_3@\text{MoS}_2$ core-shell nanowires and optimized the energy band structure by H_2 reduction to effectively reduce MoO_3 and MoS_2 interfacial defects and improve electron transfer (Fig. 11a). The constructed plasmonic $\text{MoO}_3@\text{MoS}_2$ catalyst exhibited both broadband light absorption and improved

interfacial contact, thus increasing the activity performance in water-splitting (Fig. 11b).⁹² Dong *et al.* also developed a $\text{WO}_{3-x}/\text{MoO}_{3-x}$ heterojunction catalyst with numerous oxygen vacancies, which not only enhances the optical response but also significantly facilitates electron-hole pair separation (Fig. 11c). Simultaneously, the formation of surface oxygen vacancies enhances CO_2 adsorption and activation. The results indicate that the $\text{WO}_{3-x}/\text{MoO}_{3-x}$ heterojunction greatly improves CO_2 photoreduction activity, in which CO production was $40.2 \mu\text{mol g}^{-1} \text{h}^{-1}$, approximately 9.5 times that of pure MoO_{3-x} nanosheets (Fig. 11d).⁹³

To summarize, the metallic behavior of $\text{H}_x\text{MoO}_{3-y}$ directly contributes to the photocatalytic reduction process via plasmon-induced excitation of hot electrons. On the other hand, the hot electrons are transmitted to the composite semiconductor's conduction band or to the loaded noble metal, which then participates in the reaction, boosting the catalytic activity further.

3.2. Thermal catalysis

3.2.1. CO_2 hydrogenation. Thermal catalytic CO_2 hydrogenation is a well-established technology for the conversion of CO_2 into value-added C_1 or C_{2+} species. The engineering studies of oxygen vacancy in metal oxides have been of significant attention because of their critical effects on the thermal catalytic activity of metal oxides, including facilitating the adsorption and activation of CO_2 , and a specific mechanism for providing the active species in the Mars-van Krevelen.⁹⁴ As previously stated, the orthorhombic structure of $\alpha\text{-MoO}_3$ is composed of a network of MoO_6 octahedral bilayers stacked along the [010] crystal direction, with adjacent bilayers connected through vdW forces. According to DFT calculations, the oxygen atoms (O_t) bound to Mo in the [010] crystal direction require the least energy to produce oxygen vacancies. Physical characterization reveals that oxygen vacancies typically form in the O_t position but may also form in the O_a and O_s positions with a lower probability (Fig. 12a).⁹⁵ Although the assisted activation of CO_2 molecules by oxygen vacancies in metal oxides is regarded as an attractive approach, how to maintain the concentration of oxygen vacancies in the metal oxides during the reaction is crucial to enabling the completion of a continuous catalytic cycle.^{96,97} We developed the oxygen-defective $\text{Pt}/\text{H}_x\text{MoO}_{3-y}$ catalyst to present excellent catalytic activity performance under relatively mild reaction conditions in the reaction of CO_2 hydrogenation to methanol (Fig. 12b).⁹⁸ *In situ* Mo K-edge XANES measurement investigates the average valence state of Mo, which changes reversibly in the CO_2/H_2 gas atmosphere (Fig. 12c). Pt/MoO_3 is initially reduced via an H-spillover process, producing oxygen vacancies. CO_2 is adsorbed and activated on the oxygen vacancies between the under-coordinated Mo ($\text{Mo}^{5+}/\text{Mo}^{4+}$) sites, causing the formation of CO and oxygen vacancy filling, accompanied by the oxidation of Mo atoms. Then, the oxidized Mo atoms are reduced back to the lower valence state for the regeneration of the oxygen vacancies. As the reaction timescale is extended, CO_2 is consumed continuously to create methanol, suggesting that oxygen vacancies in $\text{Pt}/\text{H}_x\text{MoO}_{3-y}$ can be stabilized during the

reaction (Fig. 12d). Therefore, a possible mechanism of CO₂ hydrogenation to methanol was proposed based on oxygen vacancy regeneration (Fig. 12e). Firstly, oxygen vacancies are produced in the H_xMoO_{3-y} during H₂ reduction (steps 1 and 2). CO₂ is adsorbed onto the oxygen vacancy and activated by the adjacent under-coordinated Mo⁵⁺/Mo⁴⁺ via high adsorption energy electron donation, weakening the C=O bond to produce *CO (step 3). The *CO intermediate migrates to the Pt nanoparticles surface (step 4) to react with the dissociated activated H species on the Pt nanoparticles to form the *COH species, which then undergoes multiple hydrogenation reactions to eventually produce methanol (step 5). Very recently, Bao *et al.* established a typical SMSI state Ru-based CO₂ hydrogenation catalyst (Ru/H_xMoO_{3-y}) that generates active molybdenum oxide in the presence of Ru metal to boost methane generation (Fig. 13a). When CO₂ hydrogenation gas at 250 °C induces the formation of a defective H_xMoO_{3-y} overlayer and eventually the encapsulated structure Ru/H_xMoO_{3-y}, product selectivity changes from 100% CH₄ selectivity on the Ru particle surface to more than 99.0% CO selectivity (Fig. 13b), and the CO₂ hydrogenation selectivity can be flipped between 99.0% CO and 100% CH₄ by cyclic reactive oxidation treatment.⁹⁹ Shimizu *et al.* discovered that Pt nanoparticles loaded on MoO_x/TiO₂ can accelerate the creation of reduced MoO_x species, hence increasing the methanol yield in the CO₂ hydrogenation reaction.¹⁰⁰ Due to molybdenum oxide's flexible

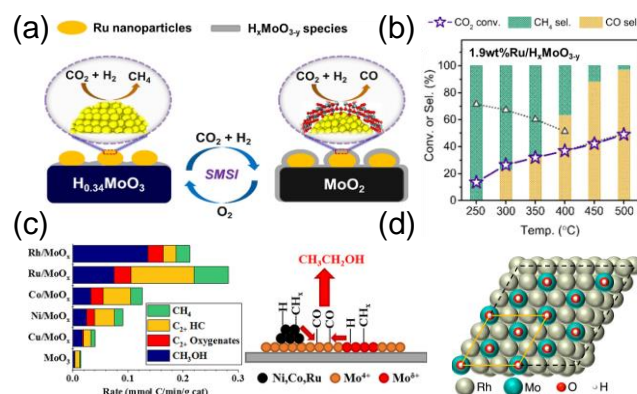


Fig. 13. (a) The mechanism of CO₂ hydrogenation reaction based on two SMSI states of Ru/H_xMoO_{3-y}. (b) Catalytic performance evolution of fresh 1.9 wt% Ru/H_xMoO_{3-y} catalyst in CO₂ hydrogenation. Copyright © 2022 American Chemical Society. (c) Activity performance in the mix gas (CO + H₂) conversion reaction and related reaction mechanism. Copyright © 2020 American Chemical Society. (d) Surface structure of 3MoOH/Rh (111) in the reaction, the orange parallelogram shows a unit. Copyright © 2019 American Chemical Society. Reproduced with permission from ref. 99, 105, 106.

redox characteristics, it can function as an active center in reverse water-gas shift (RWGS) reactions, enhancing the industrial application potential of molybdenum-based catalysts.^{101, 55} The Ti₃AlC₂ MAX phase possesses high thermal stability, toughness, and ductility like ceramics, and is also a good conductor of heat and electricity like metals. Shiju *et al.* constructed MoO₃/Ti₃AlC₂ heterojunctions and demonstrated that the existence of electron-rich Ti₃AlC₂ increases the redox characteristics of MoO₃ in the RWGS reaction, resulting in a significantly reduced surface area with a high proportion of oxygen vacancies.¹⁰²

3.2.2. CO hydrogenation. Many researchers have proved that α-MoO₃ is a novel sensing material with high sensitivity to CO gas, and this intrinsic sensing performance is derived from the presence of defects in the non-stoichiometric α-MoO₃ lattice.^{103,104} Dumesic *et al.* developed a variety of transition metal-loaded molybdenum-based catalysts for use in the conversion of mixed gases (H₂ + CO) to high-value C₂₊ oxygenates based on the properties of molybdenum oxide for CO (Fig. 13c). A series of characterizations, including H₂-D₂ exchange, temperature-programmed reaction (TPR), and XANES, indicated that spillover of activated H atoms from the noble metal to the MoO_x surface, promoting the formation of low-valent molybdenum ions and oxygen vacancies, plays a significant role in the enhanced activity. The reaction mechanism suggests that the CH_x generated at the low-valent molybdenum sites reacts with the adsorbed CO to eventually form C₂₊ oxygenates.¹⁰⁵ Although combining transition metals with MoO₃ can improve the yield of oxygenates, the structural details of the catalysts and the role of α-MoO₃ in catalytic performance are unknown. F. Bent *et al.* synthesized atomic-level precise Rh/MoO₃/SiO₂ catalysts using the ALD (atomic layer deposition) technique and investigated in detail the significance of the features of the catalyst structure in increasing catalytic performance. α-MoO₃ plays two roles: first, the existence of Mo-OH on the catalyst surface promotes CO dissociation; second, hydrogen spills over from the Mo-OH site

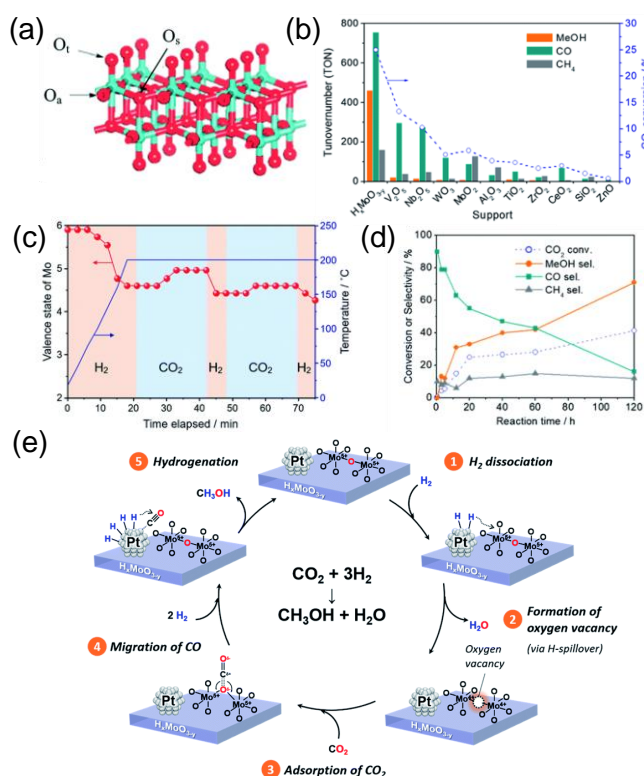


Fig. 12 (a) Possible position for the formation of different oxygen vacancies.⁹⁵ (b) The catalytic performance of several oxide-supported Pt catalysts in liquid-phase CO₂ hydrogenation. (c) valence changes of the Mo species during the *in-situ* Mo K-edge XAFS measurement. (d) Time course of the product selectivity and CO₂ conversion over Pt/H_xMoO_{3-y}. (e) Reaction mechanism for methanol production from CO₂ hydrogenation over the Pt/H_xMoO_{3-y}.⁹⁹

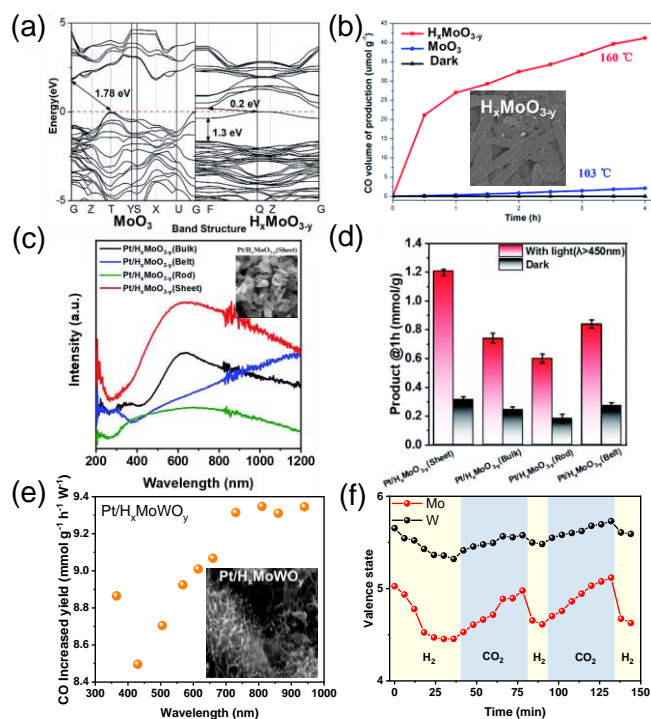


Fig. 14 (a) Calculated band structure of H_xMoO_{3-y} and MoO_3 , (b) catalytic CO generation over H_xMoO_{3-y} and MoO_3 under full-spectrum light irradiation. Reproduced with permission from ref. 114. Copyright © 2019 Royal Society of Chemistry. (c) UV-vis-NIR diffuse reflectance spectra, and (d) the CO production under visible light irradiation and in the dark over the Pt/H_xMoO_{3-y} with different morphologies.¹¹⁵ (e) Light wavelength dependence of increased CO production on Pt/H_xMoWO_y under LED light irradiation, and (f) valence changes of Mo and W species during in situ XAFS measurements.¹¹⁶

to the adsorbed species on the Rh surface, increasing the rate of hydrogenation of the reaction intermediate (Fig. 13d).¹⁰⁶ The insights obtained from the above results indicate that α - MoO_3 is an ideal material to manipulate hydrogenation reactions based on its layered structure, rich multivalent chemistry, high thermal stability, and oxygen vacancy engineering.

3.3. Photothermal catalysis

Plasmonic photothermal catalysis presents a significant difference from typical photothermal catalysis, in which the co-existence of hot electron-driven reactant activation and photothermal effects in catalysts synergistically boost surface chemistry reactions.^{107,108} The non-radiative decay of the plasmon through transitions either within the CB band or between the CB and d bands results in the generation of hot-electrons.¹⁰⁹ These hot electron-hole pairs are then transferred from the bulk of the catalyst to reactant molecules adsorbed on the surface. Furthermore, the excited hot electrons redistribute their energy through electron-phonon conversion, which leads to the heating of the catalyst surface. By intercalation of hydrogen ions and the introduction of oxygen vacancies between layers of MoO_3 , the high valent Mo^{6+} ions are reduced to Mo^{4+} and Mo^{5+} ions, thereby changing the free electron concentration of the bulk and the bandgap, conferring the H_xMoO_{3-y} a plasmonic effect, which is applied to a variety of photothermal catalysis.^{110, 111}

3.3.1. CO_2 conversion. The benefits of plasmonic photothermal catalytic CO_2 reduction are as follows: (1) Activates specific bonds of surface reactants, modifies reaction pathway, and improves selectivity;¹¹¹ (2) Facilitates the desorption process in surface catalysis to further increase catalytic activity and stability;¹¹² (3) Shifting the chemical equilibrium to a higher yield of the final product. This photothermal effect can almost entirely drive the CO_2 conversion, or in combination with the hot electron injection process, enhance the reaction collectively.¹¹³ Ye *et al.* synthesized a plasmonic H_xMoO_{3-y} by a solvothermal method, which exhibits a great potential for harnessing a wide range of visible-infrared light based on the SPR effect. The simulated energy band structure of H_xMoO_{3-y} shows that the generation of oxygen vacancies introduces defective energy levels, leading to a narrowing of the energy gap that can absorb the full spectrum (Fig. 14a). In addition, the oxygen vacancies in H_xMoO_{3-y} promote the adsorption of CO_2 molecules, lowering the barrier to CO_2 hydrogenation and photogenerated electron-hole recombination, achieving efficient thermochemical conversion in photo-thermal synergistic catalytic CO_2 reduction (Fig. 14b).¹¹⁴ The concentration of free electrons and the number of surface oxygen vacancies in MoO_3 are critical factors for the promotion of plasmonic photothermal CO_2 conversion efficiency. We found that the hybrid of Pt/H_xMoO_{3-y} with a nanosheet structure presents the best plasmonic absorption and the largest number of oxygen vacancies compared with analogues with different morphologies (bulk, rod, and belt), which can be attributed to the MoO_3 nanosheet favoring the intercalation of H^+/e^- during the H_2 reduction process (Fig. 14c). Assisted by a combination of oxygen vacancies and plasmonic absorption, Pt/H_xMoO_{3-y} (sheet) displayed the best plasmonic photothermal catalytic activity and light enhancement effects (Fig. 14d). Notably, XPS measurements demonstrate the presence of reversible redox processes involving Mo atoms during the reaction, indicating that the oxygen vacancies are active sites and regenerative.¹¹⁵ To broaden the photo-response spectrum range of plasmonic effects, we synthesized near-infrared photoexcited plasmonic Pt/H_xMoWO_y catalysts. Pt/H_xMoWO_y has a higher concentration of surface free electrons and oxygen vacancies than single Pt/H_xWO_y , which facilitates CO_2 adsorption, catalyst surface heating, and hot electron transfer processes for efficient plasmon-induced photothermal catalysis in RWGS reaction (Fig. 14e). *In situ* characterization reveals that the multivalent element Mo serves as the active center of the CO_2 conversion, with its valence increasing and decreasing in response to the creation and consumption of oxygen vacancies (Fig. 14f).¹¹⁶

3.3.2. Water purification. Utilizing the SPR effect of MoO_3 to boost photothermal conversion efficiency in order to acquire clean water from seawater and wastewater is a viable solution to the freshwater issue.^{117,118} Jiang *et al.* report that hydrogenated MoO_3 , also known as $H_{1.68}MoO_3$, is a material with a low-cost and excellent photothermal efficiency that enables efficient photothermal water evaporation throughout the solar energy spectrum (Fig. 15a). First-principles theoretical

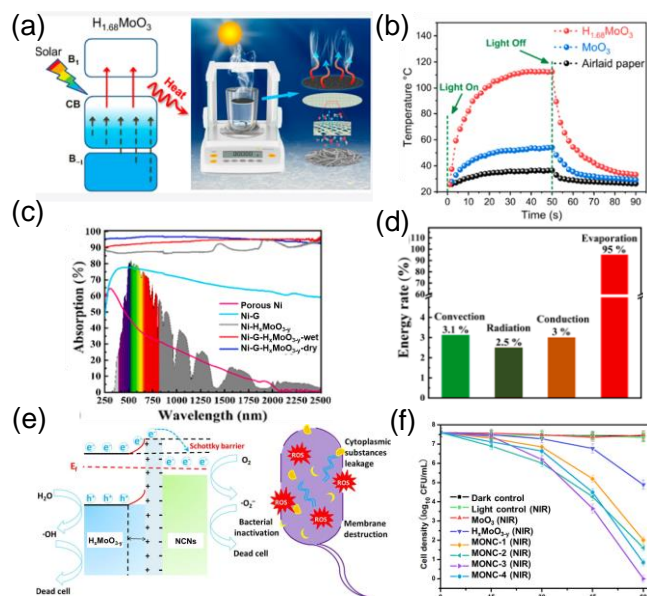


Fig. 15 (a) Schematic illustration of solar evaporation test. (b) Surface temperature of the evaporator under a solar power density of 1 kW m^{-2} . Copyright © 2019 American Chemical Society. (c) UV-vis spectra of the prepared catalyst. (d) Different energy distribution ratios of the solar evaporation process. Copyright © 2021 Elsevier. (e) The mechanisms of charge transfer and bacterial inactivation. (f) Antibacterial activities of prepared catalysts against *S. aureus* under NIR light irradiation. Copyright © 2021 Elsevier. Reproduced with permission from ref. 119, 120, 121.

calculations indicate that the transformation of the semiconductor energy band structure to a quasi-metallic structure following hydrogenation results in an insulator-to-metal phase transition, endowing $\text{H}_{1.68}\text{MoO}_3$ with broad-spectrum solar absorption and high photothermal conversion efficiency (Fig. 15b). Under solar irradiation, the interfacial evaporation system combined with the catalyst produces an unexpectedly high evaporation rate of $1.37 \text{ kg m}^{-2} \text{ h}^{-1}$.¹¹⁹ To further enhance the material's photothermal conversion efficiency, Cui *et al.* used chemical vapor deposition (CVD) and hydrothermal procedures to develop a novel catalyst composed of graphene (G) and $\text{H}_x\text{MoO}_{3-y}$ -coated porous nickel (Ni). The defective $\text{H}_x\text{MoO}_{3-y}$ increases the material's light absorption and photothermal conversion efficiency (Fig. 15c). Under solar illumination, the prepared solar evaporators exhibit great light absorption (96%), wettability, and conversion efficiency (95%) (Fig. 15d).¹²⁰ In addition, due to the growing problem of water pollution, the development of adequate catalysts for water disinfection technologies is critical for public health. Niu *et al.* recently synthesized a composite material ($\text{H}_x\text{MoO}_{3-y}/\text{NCNs}$) with near-infrared (NIR) light-triggered thermosensitive properties capable of efficiently disinfecting water, including the elimination of Enterobacteriaceae and *Staphylococcus aureus*, through the synergistic effect of photodynamic and photothermal effects (Fig. 15e, f). Studies indicate that the superior photothermal conversion efficiency (52.6%) induced by the SPR effect in the $\text{H}_x\text{MoO}_{3-y}/\text{NCNs}$ facilitates the generation of localized high temperatures that destroy bacterial cell structures.¹²¹ Unquestionably, $\alpha\text{-MoO}_3$ exhibits excellent solar energy utilization in the Vis-NIR region and contributes

significantly to the photothermal catalysis process through the thermal effect introduced by plasmonic absorption.

4. Conclusions and future prospects

In conclusion, owing to defective molybdenum oxide's unusual optical characteristics and variable multivalent state, a vast number of studies have abundantly proved its potential for a wide variety of catalytic applications, including photocatalysis, thermocatalysis, and photothermal catalysis. This article presents an overview of molybdenum oxide's crystal structure, interfacial modification, plasmonic absorption properties, and associated application advances. Taking advantage of the distinctive crystal structure of $\alpha\text{-MoO}_3$, H^+ ion intercalation and interfacial modifications are simple to achieve, resulting in plasmonic absorption and substantial surface oxygen vacancies. The defective molybdenum oxide mentioned in this paper demonstrates that strong plasmonic absorption has gained widespread interest and application in photocatalysis, effectively enhancing photocatalytic efficiency through the construction of hybrid materials and heterojunctions. Additionally, the formation of surface oxygen vacancies and the heating effect of hot electron decay extend the applicability of $\text{H}_x\text{MoO}_{3-y}$ in thermocatalysis and photothermal catalysis, where oxygen vacancies effectively adsorb and activate reactants, and the heating effect enhances the catalytic rate. In the realm of catalysis, molybdenum oxide has had remarkable success.

Although molybdenum oxide research has progressed considerably over the past decades, the catalytic mechanism still needs to be further investigated, which will allow us to develop the potential of $\text{H}_x\text{MoO}_{3-y}$ for catalytic applications in the future and to obtain catalysts with higher activity. Considering the interaction between $\text{H}_x\text{MoO}_{3-y}$ nano-structural engineering and H-spillover, multi-dimensional $\alpha\text{-MoO}_3$ materials are essential for plasmonic effects and interface engineering, particularly for the synthesis of ultrathin 2-D nanosheets and 3-D structures of $\alpha\text{-MoO}_3$, which are still incredibly challenging, but understanding the relationship between structure and photocatalytic performance is of interest for our development of $\alpha\text{-MoO}_3$ plasmonic effects. Various functionalized modifications (e.g. doping and hybridization) have also been attempted to improve the photocatalytic performance of MoO_3 , such as W-doped $\text{H}_x\text{MoO}_{3-y}$, and therefore, the development of selective doping of MoO_3 with more heterovalent atoms to improve the catalytic performance is a feasible strategy. Furthermore, the optical variations and oxygen vacancy embedding brought about by the doping of other metal oxides with Mo elements show considerable promise for catalytic applications and must be further studied. Also feasible is to apply MoO_{3-y} as a template to fabricate $\text{MoO}_{3-y}/\text{X}$ ($\text{X}=\text{S}, \text{Se}$) or multi-component heterostructures with enhanced plasmonic absorption, high defect concentration, and hot electron transfer efficiency to improve their catalytic performance in photocatalytic reactions. Importantly, according to numerous studies, the concentration of oxygen vacancies in defective molybdenum oxide plays a crucial role in photocatalysis and photothermal catalysis. It can,

to some extent, determine the electronic structure, which is vital for regulating the physicochemical properties of molybdenum oxide. In particular, precise tuning of the carrier concentrations and the corresponding changes in band structure within H_xMoO_{3-y} should be achieved to make explanations for their role in photothermal catalysis. Thus, an in-depth research is required to identify the inherent relationship between the energy band structure of defective H_xMoO_{3-y} and better catalytic performance.

In brief, defective molybdenum oxide is an excellent contender for a variety of catalytic applications and should be investigated continually for its intriguing potential. We expect that this article will contribute to a better knowledge of the optical characteristics, interface engineering, catalytic mechanism, and application prospects of defective molybdenum oxide and will serve as a springboard for future study.

Conflicts of interest

There are no conflicts to declare

Acknowledgements

The present work was supported by JST, PRESTO (Grant no. JPMJPR19T3), Japan, and a grant-in-aid for scientific research from the Japan Society for the Promotion of Science (JSPS) (no. 19H00838 and 22H00275). A part of this work was supported by the Element Strategy Initiative of MEXT, Japan (No. JPMXP0112101003).

Notes and references

- H. Ren, S. Sun, J. Cui and X. Li, *Crystal Growth & Design*, 2018, **18**, 6326–6369.
- J. Li, X. Xu, B. Huang, Z. Lou and B. Li, *ACS Appl Mater Interfaces*, 2021, **13**, 10047–10053.
- H. Sinaim, D. J. Ham, J. S. Lee, A. Phuruangrat, S. Thongtem and T. Thongtem, *Journal of Alloys and Compounds*, 2012, **516**, 172–178.
- X. Tan, L. Wang, C. Cheng, X. Yan, B. Shen and J. Zhang, *Chem Commun (Camb)*, 2016, **52**, 2893–2896.
- S. Wang, Y. Zhang, X. Ma, W. Wang, X. Li, Z. Zhang and Y. Qian, *Solid State Communications*, 2005, **136**, 283–287.
- R. Rathnasamy, R. Thangamuthu and V. Alagan, *Res Chem Intermed*, 2018, **44**, 1647–1660.
- M. L. de Sá, F. X. Nobre, L. dos S. Silva, G. da S. Sousa, M. L. Takeno, E. A. A. Júnior, J. M. E. de Matos and M. R. M. C. de Santos, *Int J Environ Res*, 2021, **15**, 105–124.
- D. J. Borah, A. T. T. Mostako and A. Malakar, *Journal of Alloys and Compounds*, 2022, **891**, 161870.
- Y. Niu, H. Su, X. Li, J. Li and Y. Qi, *Journal of Alloys and Compounds*, 2022, **898**, 162863.
- Y. Zhu, Y. Yao, Z. Luo, C. Pan, J. Yang, Y. Fang, H. Deng, C. Liu, Q. Tan, F. Liu and Y. Guo, *Molecules*, 2019, **25**, 18.
- K. Tang, S. A. Farooqi, X. Wang and C. Yan, *ChemSusChem*, 2019, **12**, 755–771.
- X. Li, D. Wang, Y. Zhang, L. Liu and W. Wang, *Nano Res.*, 2020, **13**, 3025–3032.
- H. K. Sadhanala, V. K. Harika, T. R. Penki, D. Aurbach and A. Gedanken, *ChemCatChem*, 2019, **11**, 1495–1502.
- J. Liu, G. Wang, S. Zhou, S. Liu, G. Li, H.-G. Liao and S.-G. Sun, *Journal of Energy Chemistry*, 2021, **56**, 186–192.
- K. Dossunov, G. E. Ergazieva, L. K. Myltykbaeva, M. M. Telbaeva and A. T. Batyrbaev, *Theor Exp Chem*, 2019, **55**, 137–142.
- M. Kim, J.-H. Lee and J.-M. Nam, *Advanced Science*, 2019, **6**, 1900471.
- C. Zhan, B.-W. Liu, Y.-F. Huang, S. Hu, B. Ren, M. Moskovits and Z.-Q. Tian, *Nat Commun.*, 2019, **10**, 2671.
- S. Rej, L. Mascaretti, E. Y. Santiago, O. Tomanec, Š. Kment, Z. Wang, R. Zbořil, P. Fornasiero, A. O. Govorov and A. Naldoni, *ACS Catal.*, 2020, **10**, 5261–5271.
- M. Huang, X. Wang, G. Xing, C. Meng, Y. Li, X. Li, L. Fan, Y. Wan and S. Yang, *J. Phys. Chem. Lett.*, 2021, **12**, 7988–7996.
- J. Hong, C. Xu, B. Deng, Y. Gao, X. Zhu, X. Zhang and Y. Zhang, *Advanced Science*, 2022, **9**, 2103926.
- M. Sayed, J. Yu, G. Liu and M. Jaroniec, *Chem. Rev.*, 2022, **122**, 10484–10537.
- J. Shi, Y. Kuwahara, M. Wen, M. Navlani-García, K. Mori, T. An and H. Yamashita, *Chemistry – An Asian Journal*, 2016, **11**, 2377–2381.
- L. Zheng, Y. Xu, D. Jin and Y. Xie, *Chem. Mater.*, 2009, **21**, 5681–5690.
- E. M. McCarron and J. C. Calabrese, *Journal of Solid State Chemistry*, 1991, **91**, 121–125.
- J. Yun, W. Jang, T. Lee, Y. Lee and A. Soon, *Phys. Rev. Applied*, 2017, **7**, 024025.
- D. D. Yao, J. Z. Ou, K. Latham, S. Zhuiykov, A. P. O'Mullane and K. Kalantar-zadeh, *Crystal Growth & Design*, 2012, **12**, 1865–1870.
- K. Kalantar-zadeh, J. Tang, M. Wang, K. L. Wang, A. Shailos, K. Galatsis, R. Kojima, V. Strong, A. Lech, W. Wlodarski and R. B. Kaner, *Nanoscale*, 2010, **2**, 429–433.
- F. Ji, X. Ren, X. Zheng, Y. Liu, L. Pang, J. Jiang and S. (Frank) Liu, *Nanoscale*, 2016, **8**, 8696–8703.
- D. O. Scanlon, G. W. Watson, D. J. Payne, G. R. Atkinson, R. G. Egdell and D. S. L. Law, *J. Phys. Chem. C*, 2010, **114**, 4636–4645.
- C. Wu, H. Xie, D. Li, D. Liu, S. Ding, S. Tao, H. Chen, Q. Liu, S. Chen, W. Chu, B. Zhang and L. Song, *J. Phys. Chem. Lett.*, 2018, **9**, 817–824.
- X. Hu, W. Zhang, X. Liu, Y. Mei and Y. Huang, *Chem. Soc. Rev.*, 2015, **44**, 2376–2404.
- L. Q. Mai, B. Hu, W. Chen, Y. Y. Qi, C. S. Lao, R. S. Yang, Y. Dai and Z. L. Wang, *Advanced Materials*, 2007, **19**, 3712–3716.
- X. K. Hu, Y. T. Qian, Z. T. Song, J. R. Huang, R. Cao and J. Q. Xiao, *Chem. Mater.*, 2008, **20**, 1527–1533.
- X. Sha, L. Chen, A. C. Cooper, G. P. Pez and H. Cheng, *J. Phys. Chem. C*, 2009, **113**, 11399–11407.
- B. Y. Zhang, A. Zavabeti, A. F. Chrimes, F. Haque, L. A. O'Dell, H. Khan, N. Syed, R. Datta, Y. Wang, A. S. R. Chesman, T. Daeneke, K. Kalantar-zadeh and J. Z. Ou, *Advanced Functional Materials*, 2018, **28**, 1706006.
- B. Braïda, S. Adams and E. Canadell, *Chem. Mater.*, 2005, **17**, 5957–5969.
- L. Xie, T. Chen, H. C. Chan, Y. Shu and Q. Gao, *Chemistry – An Asian Journal*, 2018, **13**, 641–647.
- L. Xie, Q. Zhu, G. Zhang, K. Ye, C. Zou, O. V. Prezhdo, Z. Wang, Y. Luo and J. Jiang, *J. Am. Chem. Soc.*, 2020, **142**, 4136–4140.
- J. Yang, F. Lu, Y. Li, S. Yang, R. Li, N. Huo, C. Fan, Z. Wei, J. Li and S.-S. Li, *Journal of Materials Chemistry C*, 2014, **2**, 1034–1040.
- Q. Huang, S. Hu, J. Zhuang and X. Wang, *Chemistry – A European Journal*, 2012, **18**, 15283–15287.
- S. Xie, H. Zhang, G. Liu, X. Wu, J. Lin, Q. Zhang and Y. Wang, *Chinese Journal of Catalysis*, 2020, **41**, 1125–1131.
- E. B. Kadossov, A. R. Soufiani, A. W. Apblett and N. F. Materer, *RSC Adv.*, 2015, **5**, 97755–97763.

- 43 J. N. Yao, K. Hashimoto and A. Fujishima, *Nature*, 1992, **355**, 624–626.
- 44 J. Balach, J. Linnemann, T. Jaumann and L. Giebeler, *Journal of Materials Chemistry A*, 2018, **6**, 23127–23168.
- 45 H.-S. Kim, J. B. Cook, H. Lin, J. S. Ko, S. H. Tolbert, V. Ozolins and B. Dunn, *Nature Mater*, 2017, **16**, 454–460.
- 46 V. Agarwal and H. Metiu, *J. Phys. Chem. C*, 2016, **120**, 19252–19264.
- 47 A. Agrawal, S. H. Cho, O. Zandi, S. Ghosh, R. W. Johns and D. J. Milliron, *Chem. Rev.*, 2018, **118**, 3121–3207.
- 48 J. M. Luther, P. K. Jain, T. Ewers and A. P. Alivisatos, *Nature Mater*, 2011, **10**, 361–366.
- 49 M. Hu, J. Chen, Z.-Y. Li, L. Au, G. V. Hartland, X. Li, M. Marquez and Y. Xia, *Chem. Soc. Rev.*, 2006, **35**, 1084–1094.
- 50 S. Qi, G. Liu, L. Tan, J. Chen, Y. Lou and Y. Zhao, *Chem. Commun.*, 2020, **56**, 4816–4819.
- 51 X. Li, D. Wang, Y. Zhang, L. Liu and W. Wang, *Nano Res.*, 2020, **13**, 3025–3032.
- 52 M. K. Patil, S. H. Gaikwad and S. P. Mukherjee, *J. Phys. Chem. C*, 2020, **124**, 21082–21093.
- 53 T. He and J. Yao, *Journal of Photochemistry and Photobiology C: Photochemistry Reviews*, 2003, **4**, 125–143.
- 54 T. Ressler, R. E. Jentoft, J. Wienold, M. M. Günter and O. Timpe, *J. Phys. Chem. B*, 2000, **104**, 6360–6370.
- 55 A. Borgschulte, O. Sambalova, R. Delmelle, S. Jenatsch, R. Hany and F. Nüesch, *Sci. Rep.*, 2017, **7**, 40761.
- 56 H. Cheng, M. Wen, X. Ma, Y. Kuwahara, K. Mori, Y. Dai, B. Huang and H. Yamashita, *J. Am. Chem. Soc.*, 2016, **138**, 9316–9324.
- 57 F. Wang, Q. Li, L. Lin, H. Peng, Z. Liu and D. Xu, *J. Am. Chem. Soc.*, 2015, **137**, 12006–12012.
- 58 Y. Kuwahara, M. Okada, H. Ge and H. Yamashita, *Chem. Lett.*, 2022, **51**, 166–169.
- 59 C. Zhan, X.-J. Chen, J. Yi, J.-F. Li, D.-Y. Wu and Z.-Q. Tian, *Nat. Rev. Chem.*, 2018, **2**, 216–230.
- 60 P. Narang, R. Sundararaman and H. A. Atwater, *Nanophotonics*, 2016, **5**, 96–111.
- 61 D. B. Ingram and S. Linic, *J. Am. Chem. Soc.*, 2011, **133**, 5202–5205.
- 62 D. B. Ingram, P. Christopher, J. L. Bauer and S. Linic, *ACS Catal.*, 2011, **1**, 1441–1447.
- 63 S. Linic, P. Christopher and D. B. Ingram, *Nature Mater*, 2011, **10**, 911–921.
- 64 H. Fang, M. Hegde, P. Yin and P. V. Radovanovic, *Chem. Mater.*, 2017, **29**, 4970–4979.
- 65 J. Li, G. Chen, J. Yan, B. Huang, H. Cheng, Z. Lou and B. Li, *Applied Catalysis B: Environmental*, 2020, **264**, 118517.
- 66 K. Manthiram and A. P. Alivisatos, *J. Am. Chem. Soc.*, 2012, **134**, 3995–3998.
- 67 Y. Zhao, H. Pan, Y. Lou, X. Qiu, J. Zhu, and C. Burda, *J. Am. Chem. Soc.*, 2009, **131**, 4253–4261.
- 68 M. L. Brongersma, N. J. Halas and P. Nordlander, *Nature Nanotech*, 2015, **10**, 25–34.
- 69 H. Cheng, T. Kamegawa, K. Mori and H. Yamashita, *Angewandte Chemie*, 2014, **126**, 2954–2958.
- 70 Z. Wang, X. Wang, E. Sharman, X. Li, L. Yang, G. Zhang and J. Jiang, *J. Phys. Chem. Lett.*, 2020, **11**, 1075–1080.
- 71 H. Yin, Y. Kuwahara, K. Mori, H. Cheng, M. Wen and H. Yamashita, *Journal of Materials Chemistry A*, 2017, **5**, 8946–8953.
- 72 N. J. Kramer, K. S. Schramm and U. R. Kortshagen, *Nano Lett.*, 2015, **15**, 5597–5603.
- 73 S. Zhou, Z. Ni, Y. Ding, M. Sugaya, X. Pi and T. Nozaki, *ACS Photonics*, 2016, **3**, 415–422.
- 74 E. Della Gaspera, A. S. R. Chesman, J. van Embden and J. J. Jasieniak, *ACS Nano*, 2014, **8**, 9154–9163.
- 75 H. Yin, Y. Kuwahara, K. Mori, H. Cheng, M. Wen, Y. Huo and H. Yamashita, *J. Phys. Chem. C*, 2017, **121**, 23531–23540.
- 76 J. Shi, *Chem. Rev.*, 2013, **113**, 2139–2181.
- 77 R. Jiang, B. Li, C. Fang and J. Wang, *Advanced Materials*, 2014, **26**, 5274–5309.
- 78 Y. Kuwahara, Y. Yoshimura, K. Haematsu and H. Yamashita, *J. Am. Chem. Soc.*, 2018, **140**, 9203–9210.
- 79 H. Cheng, X. Qian, Y. Kuwahara, K. Mori and H. Yamashita, *Advanced Materials*, 2015, **27**, 4616–4621.
- 80 H. Yin, Y. Kuwahara, K. Mori, M. Che and H. Yamashita, *J. Mater. Chem. A*, 2019, **7**, 3783–3789.
- 81 H. Yin, Y. Kuwahara, K. Mori and H. Yamashita, *European Journal of Inorganic Chemistry*, 2019, **2019**, 3745–3752.
- 82 Z. Bian, T. Tachikawa, P. Zhang, M. Fujitsuka and T. Majima, *J. Am. Chem. Soc.*, 2014, **136**, 458–465.
- 83 J.-D. Xiao, L. Han, J. Luo, S.-H. Yu and H.-L. Jiang, *Angew Chem Int Ed Engl*, 2018, **57**, 1103–1107.
- 84 H. Jun, S. Choi, M. Y. Yang and Y. S. Nam, *J. Mater. Chem. A*, 2019, **7**, 17254–17260.
- 85 M. Wen, S. Song, Q. Liu, H. Yin, K. Mori, Y. Kuwahara, G. Li, T. An and H. Yamashita, *Applied Catalysis B: Environmental*, 2021, **282**, 119511.
- 86 K. S. Novoselov, A. Mishchenko, A. Carvalho and A. H. Castro Neto, *Science*, 2016, **353**, aac9439.
- 87 J. Kou, C. Lu, J. Wang, Y. Chen, Z. Xu and R. S. Varma, *Chem. Rev.*, 2017, **117**, 1445–1514.
- 88 M. Shahrokhi, P. Raybaud and T. Le Bahers, *ACS Appl. Mater. Interfaces*, 2021, **13**, 36465–36474.
- 89 J. Peng, J. Shen, X. Yu, H. Tang, Zulfiqar and Q. Liu, *Chinese Journal of Catalysis*, 2021, **42**, 87–96.
- 90 X. Tan, J. Melkersson, S. Wu, L. Wang and J. Zhang, *ChemPhysChem*, 2016, **17**, 2630–2639.
- 91 X. Liu and M. T. Swihart, *Chemical Society Reviews*, 2014, **43**, 3908–3920.
- 92 S. Guo, X. Li, X. Ren, L. Yang, J. Zhu and B. Wei, *Advanced Functional Materials*, 2018, **28**, 1802567.
- 93 Y. Liu, X. Dong, Q. Yuan, J. Liang, Y. Zhou, X. Qu and B. Dong, *Colloids and Surfaces A: Physicochemical and Engineering Aspects*, 2021, **621**, 126582.
- 94 H. Zhang, Z. Zhang, Y. Liu, X. Fang, J. Xu, X. Wang and X. Xu, *J. Phys. Chem. Lett.*, 2021, **12**, 9188–9196.
- 95 H. Yin, Y. Kuwahara, K. Mori, H. Cheng, M. Wen, Y. Huo and H. Yamashita, *J. Phys. Chem. C*, 2017, **121**, 23531–23540.
- 96 M. S. Frei, C. Mondelli, R. García-Muelas, K. S. Kley, B. Puértolas, N. López, O. V. Safonova, J. A. Stewart, D. Curulla Ferré and J. Pérez-Ramírez, *Nat Commun*, 2019, **10**, 3377.
- 97 K. Larmier, W.-C. Liao, S. Tada, E. Lam, R. Verel, A. Bansode, A. Urakawa, A. Comas-Vives and C. Copéret, *Angewandte Chemie International Edition*, 2017, **56**, 2318–2323.
- 98 Y. Kuwahara, T. Mihogi, K. Hamahara, K. Kusu, H. Kobayashi and H. Yamashita, *Chem. Sci.*, 2021, **12**, 9902–9915.
- 99 H. Xin, L. Lin, R. Li, D. Li, T. Song, R. Mu, Q. Fu and X. Bao, *J. Am. Chem. Soc.*, 2022, **144**, 4874–4882.
- 100 T. Toyao, S. Kayamori, Z. Maeno, S. M. A. H. Siddiki and K. Shimizu, *ACS Catal.*, 2019, **9**, 8187–8196.
- 101 S. Omotayo Akande, A. Chronos, M. Vasilopoulou, S. Kennou and U. Schwingenschlögl, *Journal of Materials Chemistry C*, 2016, **4**, 9526–9531.
- 102 M. Ronda-Lloret, L. Yang, M. Hammerton, V. S. Marakatti, M. Tromp, Z. Sofer, A. Sepúlveda-Escribano, E. V. Ramos-Fernandez, J. J. Delgado, G. Rothenberg, T. Ramirez Reina and N. R. Shiju, *ACS Sustainable Chem. Eng.*, 2021, **9**, 4957–4966.
- 103 S. Bai, C. Chen, Y. Tian, S. Chen, R. Luo, D. Li, A. Chen and C. C. Liu, *Materials Research Bulletin*, 2015, **64**, 252–256.
- 104 K. Xu, N. Liao, B. Zheng and H. Zhou, *Physics Letters A*, 2020, **384**, 126533.
- 105 L. Zhang, M. R. Ball, K. R. Rivera-Dones, S. Wang, T. F. Kuech, G. W. Huber, I. Hermans and J. A. Dumesic, *ACS Catal.*, 2020, **10**, 365–374.

- 106 A. S. Asundi, A. S. Hoffman, P. Bothra, A. Boubnov, F. D. Vila, N. Yang, J. A. Singh, L. Zeng, J. A. Raiford, F. Abild-Pedersen, S. R. Bare and S. F. Bent, *J. Am. Chem. Soc.*, 2019, **141**, 19655–19668.
- 107 S. Luo, H. Song, D. Philo, M. Oshikiri, T. Kako and J. Ye, *Applied Catalysis B: Environmental*, 2020, **272**, 118965.
- 108 N. Keller, J. Ivanez, J. Highfield and A. M. Ruppert, *Applied Catalysis B: Environmental*, 2021, **296**, 120320.
- 109 Y. Zhang, S. He, W. Guo, Y. Hu, J. Huang, J. R. Mulcahy and W. D. Wei, *Chem. Rev.*, 2018, **118**, 2927–2954.
- 110 U. Aslam, V. G. Rao, S. Chavez and S. Linic, *Nat Catal*, 2018, **1**, 656–665.
- 111 E. Cortés, *Advanced Optical Materials*, 2017, **5**, 1700191.
- 112 Z. Wang, H. Song, H. Liu and J. Ye, *Angewandte Chemie International Edition*, 2020, **59**, 8016–8035.
- 113 Y. Bai, J. Zhao, S. Feng, X. Liang and C. Wang, *Chem. Commun.*, 2019, **55**, 4651–4654.
- 114 J. Li, Y. Ye, L. Ye, F. Su, Z. Ma, J. Huang, H. Xie, D. E. Doronkin, A. Zimina, J.-D. Grunwaldt and Y. Zhou, *J. Mater. Chem. A*, 2019, **7**, 2821–2830.
- 115 H. Ge, Y. Kuwahara, K. Kusu and H. Yamashita, *Journal of Materials Chemistry A*, 2021, **9**, 13898–13907.
- 116 H. Ge, Y. Kuwahara, K. Kusu, H. Kobayashi and H. Yamashita, *Journal of Materials Chemistry A*, 2022, **10**, 10854–10864.
- 117 Q. Chen, Z. Pei, Y. Xu, Z. Li, Y. Yang, Y. Wei and Y. Ji, *Chem. Sci.*, 2018, **9**, 623–628.
- 118 M. Gao, P. K. N. Connor and G. W. Ho, *Energy Environ. Sci.*, 2016, **9**, 3151–3160.
- 119 Q. Zhu, K. Ye, W. Zhu, W. Xu, C. Zou, L. Song, E. Sharman, L. Wang, S. Jin, G. Zhang, Y. Luo and J. Jiang, *J. Phys. Chem. Lett.*, 2020, **11**, 2502–2509.
- 120 L. Gong, C. Li, N. Wei, J. Li, J. Shen, R. Xu, Q. Li, J. Tian and H. Cui, *Separation and Purification Technology*, 2021, **275**, 119139.
- 121 Y.-Y. Yang, H.-P. Feng, C.-G. Niu, D.-W. Huang, H. Guo, C. Liang, H.-Y. Liu, S. Chen, N. Tang and L. Li, *Chemical Engineering Journal*, 2021, **426**, 131902.